nature nanotechnology

LETTERS

PUBLISHED ONLINE: 17 OCTOBER 2010 | DOI: 10.1038/NNANO.2010.196

Exciton-like trap states limit electron mobility in TiO_2 nanotubes

Christiaan Richter† and Charles A. Schmuttenmaer*

Nanoparticle films have become a promising low-cost, high-surface-area electrode material for solar cells and solar fuel production[1,2]. Compared to sintered nanoparticle films, oriented polycrystalline titania nanotubes offer the advantage of directed electron transport, and are expected to have higher electron mobility[3–7]. However, macroscopic measurements have revealed their electron mobility to be as low as that of nanoparticle films[8,9]. Here, we show, through time-resolved terahertz spectroscopy[10], that low mobility in polycrystalline TiO_2 nanotubes is not due to scattering from grain boundaries or disorder-induced localization as in other nanomaterials[11,12], but instead results from a single sharp resonance arising from exciton-like trap states. If the number of these states can be lowered, this could lead to improved electron transport in titania nanotubes and significantly better solar cell performance.

Alternative energy sources such as those based on solar power must be developed in order to cut back on greenhouse gas emissions and move away from fossil fuels, and in the last two decades there has been an ever increasing effort to make use of nanomaterials in alternative solar cell designs. One such nanomaterial, discovered in 2001, is composed of ordered titania nanotubes[13]. It has been proposed that anodic titania nanotubes may have unique electron transport properties that make them an enabling technology for next-generation solar cells[4,14,15], including dye-sensitized solar cells (DSSCs)[4–6], and in photoelectrochemical cells for the production of solar hydrogen[16,17]. Both applications require that free carriers (electrons) be transported through an anodic TiO_2 electrode, either along the length of nanotubes in the case of nanotube electrodes, or through a porous nanoparticle network by means of a random walk in standard DSSCs[2,3,8]. Several authors have suggested that nanotubes would be superior to nanoparticle networks regarding the vectorial electron transport required in applications such as DSSCs[5,6,18]. However, whole-cell evaluation of electron mobility through nanotubes has found that they are not much better than nanoparticle films[8]. In this study we use time-resolved terahertz spectroscopy (TRTS) to directly probe and reveal the microscopic electron transport properties of nanotube arrays.

We have previously used TRTS to directly probe electron transport in TiO_2 nanoparticle films[12]. TRTS revealed that electrons are surprisingly mobile within nanoparticles, but that transport through the nanoparticle film is impeded by the strong backscattering and/or disorder-induced localization of electrons. In other words, electron localization involves the whole particle and thus suggests structural disorder as being the dominant impediment to transport in nanoparticle films.

Ordered TiO_2 nanotubes are fabricated by anodizing titanium foil in an electrolyte containing fluoride or chloride, as described in the Methods[4–9,13,15–18]. The halogen anions in the electrolyte disrupt passivation during the electrochemical oxidation of the titanium foil, resulting in the formation of nanotubes (Fig. 1) as the metal foil is transformed into the oxide[15,18]. The as-anodized nanotube films are amorphous and are subsequently transformed into polycrystalline anatase by low-temperature annealing[4–9,13,15–18].

Here, we probe electron injection, cooling and transport in TiO_2 nanotubes on a sub-picosecond timescale using TRTS. We find that, unlike nanoparticles, there is no evidence of significant backscattering or disorder-induced localization. Instead, the conductivity spectrum of the nanotubes reveals a distinct resonance at ~7.5 meV, which corresponds to an exciton-like entity. Hence, even though macroscopic measurements have shown similarly low electron mobilities in TiO_2 nanoparticles when compared to nanotube films, the underlying reasons for this are very different.

In previous work we obtained the frequency-dependent complex photoconductivity, $\hat{\sigma}(\omega) = \sigma_1(\omega) + i\sigma_2(\omega)$, of rutile single crystals and nanoparticle films over terahertz frequencies[12]. As can be seen in Fig. 2 the single crystal demonstrates ideal Drude conductivity. On the other hand, anatase and rutile nanoparticle films of various sizes (7–200 nm)[12,19,20], as well as ZnO nanoparticle and nanowire films[11], do not all conform to classical Drude behavior, but instead demonstrate behaviour that can be consistently fit by the extended Drude–Smith model[12,19,21,22]. In all of these samples, the imaginary conductivity, $\sigma_2(\omega)$, is negative at low frequencies, corresponding to a Drude–Smith parameter c close to –1, which suggests transport dominated by backscattering and/or disorder-induced localization.

A representative $\hat{\sigma}(\omega)$ spectrum for TiO_2 nanotubes is also shown in Fig. 2. In both the nanotube and nanoparticle samples, d.c. conductivity is suppressed, that is, $\sigma_{1,dc,nano} \ll \sigma_{1,dc,crystal}$, as $\omega \to 0$ (where σ_1 is the real part of the complex-valued conductivity), suggesting comparably low electron mobility. However, the nanotube spectrum is fundamentally different from that for single-crystal or nanoparticulate TiO_2, and is dominated by a sharp resonance at ~1.8 THz (7.5 meV). Even though the experimental bandwidth extends only up to 1.6 THz when probing the single crystal and nanoparticle samples, it is clear from the lack of downward curvature in σ_2 that no oscillator component is present. Furthermore, Tiwana and colleagues recently measured the TiO_2 nanoparticle photoconductivity spectrum to 2.0 THz and did not observe a resonant feature[20] (see Supplementary Information for a detailed discussion).

As can be seen in Fig. 3 and the plots in the Supplementary Information, the resonance at 1.8 THz is present in all polycrystalline nanotube samples, whether annealed at 400 °C or 475 °C, whether stained with N3 (also known as red dye) and photoexcited at 400 nm, or N749 (also known as black dye) and photoexcited at 800 nm. The observed resonance can be fit in all spectra by a single classical Lorentz oscillator (see Supplementary Information for fitting equations and parameter values obtained). Our $\hat{\sigma}(\omega)$

Department of Chemistry, Yale University, 225 Prospect St., New Haven, Connecticut 06520-8107 USA; †Present address: Rochester Institute of Technology, Chemical and Biomedical Engineering, 160 Lomb Memorial Drive, Rochester, New York 14623-5603 USA.
*e-mail: charles.schmuttenmaer@yale.edu

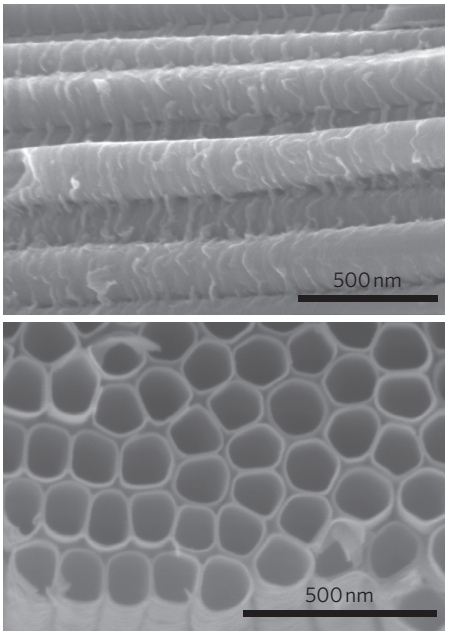

Figure 1 | Scanning electron microscopy images of TiO_2 nanotube arrays fabricated by anodization.

spectra closely resemble those of Kaindl and colleagues[23] who probed an electron–hole plasma generated in GaAs quantum wells using TRTS to observe a virtually instantaneous exciton correlation between electrons and holes, and subsequent formation of insulating excitons.

The non-resonant component of $\sigma_1(\omega)$ in our spectra is well approximated by a power-law dependence ($\sigma_1(\omega) \propto \omega^{\alpha}$) as is typical of disorder-inhibited transport[12,24,25]. Others have proposed the extension of a power-law-dependent real conductivity, $\sigma_1(\omega)$, to complex conductivity[24,25], which is consistent with the Kramers–Krönig relations:

$$\sigma_{PL}(\omega) = A\left(i\frac{\omega}{\omega_s}\right)^{\alpha} \quad (1)$$

where A is a scaling factor and ω_s is an arbitrary frequency scale (we choose $\omega_s = 2\pi \cdot 1$ THz). We find that using this form, together with a Lorentz oscillator at ~1.8 THz, results in excellent fits of both the real and imaginary parts of all $\hat{\sigma}(\omega)$ spectra taken using a minimal number of fitting parameters (see Fig. 3 and Supplementary Tables S1–S3).

Experiments[26–28] and simulations[29] suggest that isolated Ti^{3+} sites will have a ground-state energy level ~1 eV below the conduction band (CB) edge (Supplementary Fig. S5). However, high-energy photoelectron spectroscopy and optical spectroscopy reveal that these states are present in a high enough density to form impurity bands that extend virtually all the way to the CB edge[26–28]. The presence of these bands raises the Fermi level, and a sizeable fraction of Ti^{3+} states are thermally ionized at room temperature, and are denoted $Ti^{4+\star}$. This notation is used to distinguish it from Ti^{4+}, the usual oxidation state of Ti in TiO_2 in the absence of oxygen vacancies. This results in a measurable room-temperature conductivity for anatase, and a corresponding number of positively charged ionized donor sites ($[Ti^{4+\star}] \approx 1 \times 10^{18}$ cm^{-3})[30–32].

The hydrogenic model used for estimating the binding energy of excitons[23] is equally applicable to the interaction of free electrons and donor impurities, provided the exciton reduced mass is replaced by the electron effective mass:

$$E_n = -\frac{m_e}{m_0}\frac{1}{\varepsilon_R^2}\frac{R_H}{n^2} \quad (2)$$

where m_e is the electron effective mass (~$4m_0$)[32,33], m_0 the free electron mass, ε_R the relative dielectric constant (measured by TRTS to be ~70) and R_H the hydrogen atom Rydberg energy (13.6 eV). Using these values, a binding energy E_{BE} of 11.2 meV is calculated, leading to a $n = 1 \rightarrow n = 2$ transition energy of 8.4 meV. At 293 K, 32% of these 'excitons' will be bound.

Before photoexcitation there exists an equilibrium between bound and ionized excitons:

$$[Ti^{4+\star}/e^-] \rightleftharpoons [e^-][Ti^{4+\star}] \quad (3)$$

Within several hundreds of femtoseconds after photoexcitation of a dye-sensitized sample, the excited dyes inject more than 1×10^{18} cm^{-3} free electrons into the TiO_2, roughly doubling the free carrier electron density. As a result of the equilibrium shown in equation (3), this will also significantly increase the concentration of $Ti^{4+\star}/e^-$, and, therefore, the resonant feature is observed even at room temperature.

The fact that the same resonance has not been observed in nanoparticle films arises because they have a lower Ti^{3+} concentration (a more detailed discussion is given in the Supplementary Information). The Ti^{3+} donor states can result from oxygen vacancies, titanium interstitials that may result from an excess of titanium during fabrication (the nanotubes are made from pure titanium foil) and/or substitutional fluoride impurities (fluoride is a necessary ingredient in the nanotube fabrication process). The most likely origins of these defect states in nanotubes are therefore the unique fabrication techniques used to make anodic nanotubes (titanium excess and F^- anions). A common strategy for eliminating these defects is annealing at elevated temperatures in an oxygen-rich

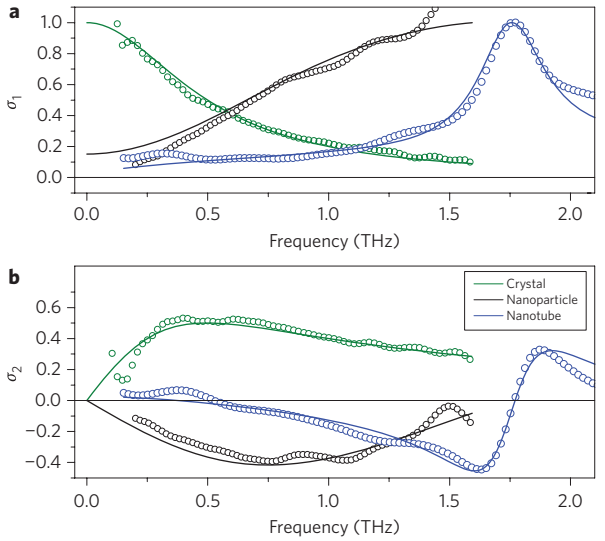

Figure 2 | Frequency-dependent photoconductivities. a,**b**, Real (**a**) and imaginary (**b**) photoconductivities of rutile single crystal (green), Degussa P25 nanoparticle film (black) and nanotube sample (blue). All samples were stained with N3 dye, and the terahertz spectra were taken within 10 ps after photoexcitation with a 400-nm pulse. The data (open circles) are fit by the standard Drude model for the single crystal, the Drude–Smith model for the nanoparticles, and a Lorentz oscillator plus power law conductivity for the nanotubes. All spectra are scaled to the maximum of their respective $\sigma_1(\omega)$ for comparison.

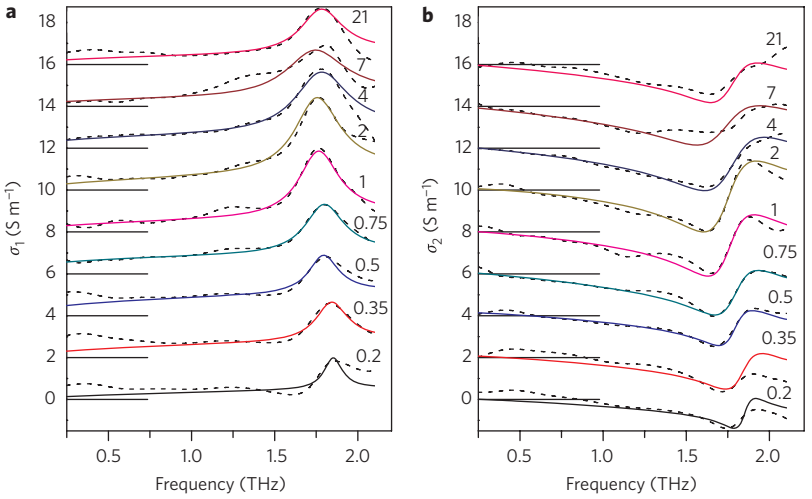

Figure 3 | Photoconductivity of a TiO_2 nanotube sample. a,**b**, Real (**a**) and imaginary (**b**) photoconductivities of a TiO_2 nanotube sample (400 °C anneal for 1 h, stained with N3 dye). Data (dotted lines) and best fits to the data (solid lines) are shown. The spectra are offset by 2 S m^{-1} from each other and labelled with the time in picoseconds after photoexcitation (0.2–21 ps) by a 400-nm pulse. Similar plots for samples annealed at higher temperature (475 °C) and photoexcited at both 400 and 800 nm may be seen in the Supplementary Information.

environment[14,34,35]. Unfortunately, the nanotubes begin to lose their structural integrity at 500−550 °C, limiting the annealing temperature, and with it possibly the ability to remove oxygen vacancies. Another difference between the nanotube and nanoparticle samples is that the nanotubes are most likely a compensated n-type semiconductor due to the presence and possible doping with small amounts of C and N atoms[14] (see Supplementary Information). The Fermi level in the nanotubes could therefore be somewhat lower than that of the pure n-type nanoparticles, which would lead to a larger observed shallow donor resonance in the nanotubes, as discussed in the Supplementary Information.

Finally, the time dependence of the conductivity is considered. All samples have an instrument response-limited onset of terahertz absorption that is completed within ∼400 fs. The amplitude of the resonance reaches a maximum within the first 2 ps and then decays to a lower plateau value over the next ∼5–10 ps (Supplementary Figs S6,S7). Figure 4 shows a plot of the scattering rate, γ, of the exciton-like states as a function of pump/probe delay time. The peak width (full-width at half-maximum) is $\gamma/2\pi$. Carriers injected from N3 dye into TiO_2 are hot, and typically equilibrate with the lattice within a few hundred femtoseconds to picoseconds. In nanoparticles, this cooling corresponds to a decrease in the electron scattering rate and a decrease in the 'backscattering' parameter on a 500-fs timescale[12]. In nanotubes, the timescale for carrier-lattice equilibration is ∼10–50 times longer, and the 'free' carriers pass through these exciton-like states on their way to either being trapped in deep traps or recombining with an oxidized dye molecule. Increasing the anneal temperature from 400 to 475 °C increases the crystallinity and slows the timescale for equilibration (red curve in Fig. 4).

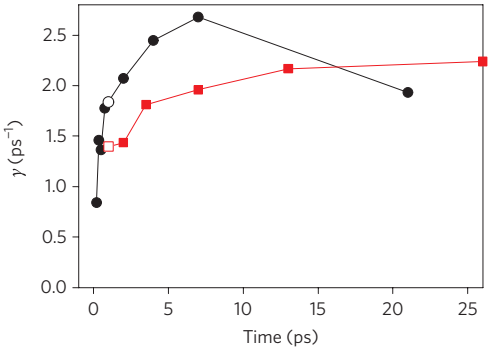

Figure 4 | Fitting parameter γ as a function of time after photoexcitation. Black filled circles represent data for a sample annealed at 400 °C, and red squares a sample annealed at 475 °C. The open symbols are those at a delay time of 1 ps.

In conclusion, macroscopic measurements show that TiO_2 nanotube and nanoparticle films have equally low electron transport when used in DSSCs[8,9]. TRTS measurements of the photoconductivity in nanotube films presented here confirm the comparably low electron mobility of nanoparticle and nanotube films. In nanoparticle films, conductivity is inhibited by significant backscattering and/or disorder-induced localization. In nanotube films, the photoconductivity spectrum is dominated by a relatively sharp resonance at ∼7.5 meV. These findings suggest that if the number of Ti^{3+} states can be lowered, most likely by altering the fabrication procedure, then TiO_2 nanotubes would have superior electron transport properties compared to nanoparticle films and could lead to significantly better DSSC performance.

Methods

Nanotube fabrication. Titania nanotube arrays were fabricated by anodizing titanium foil (200 μm thick, Strem Chemicals) in a two-electrode cell[8,17]. The counterelectrode comprised platinum mesh, with an electrode spacing of 5 cm. The electrolyte was 0.15 M NH_4F, with 6 vol% deionized water in ethylene glycol. Samples were anodized at 50 V for 50 h under nitrogen. Subsequently samples were annealed at either 400 or 475 °C for 1 h. The average nanotube dimensions, as determined by scanning electron microscopy, were 42±1.4 μm (length), 150±9.5 nm (diameter) and 28±2.2 nm (wall thickness). To perform terahertz spectroscopy, the titanium metal substrate of the titania nanotube arrays was removed. This was done by mounting the sample in a flat cell with the metal substrate of the nanotubes contacting an etching electrolyte. The samples were then electrochemically etched for ∼45 min until they became transparent (that is, the metallic layer below the nanotube array was completely removed). The etching electrolyte was 0.2 M KBr, and the applied bias was 7 V. The electrolyte was vigorously stirred during etching using a magnetic stirrer to prevent the build-up of etching products. Samples were stained with N3 ($RuL_2(NCS)_2$; L = 2,2′-bipyridyl-4,4′-dicarboxylic acid) or N749 ($RuL'(NCS)_3$; L′ = 2,2′,2″-terpyridyl-4,4′,4″-tricarboxylic acid) by soaking them overnight in a 0.6 mM solution of the dye in ethanol.

Pump–probe terahertz spectroscopy. An amplified Ti:sapphire laser (Tsunami/Spitfire, Spectra Physics) was used to generate 800 mW of pulsed near-infrared light at 1 kHz. The pulse width was ∼100 fs, and the centre wavelength was 800 nm. About two-thirds of the power was frequency-doubled to produce 150 mW (60 mW at the sample) of 400 nm light for the pump beam. The remainder of the near-infrared light was used to generate and detect terahertz radiation using a

four-paraboloid arrangement that focused the terahertz radiation to a spot size of ~3 mm at the sample. Terahertz radiation was generated using optical rectification in a ZnTe crystal and detected using free-space electrooptic sampling in a second ZnTe crystal. More details on the TRTS spectrometer have been published elsewhere[10,12]. By measuring the full transmitted terahertz field, the complex dielectric constant of the sample was calculated. Thereafter, the photoconductivity/complex dielectric constant of the photoexcited sample was calculated for various pump–probe delay times[11,12] (see Supplementary Information).

Received 21 May 2010; accepted 7 September 2010; published online 17 October 2010

References

1. O'Regan, B. & Grätzel, M.A. Low-cost, high-efficiency solar cell based on dye-sensitized colloidal TiO_2 films. *Nature* **353,** 737–740 (1991).
2. Gratzel, M. Photoelectrochemical cells. *Nature* **414,** 338–344 (2001).
3. Kopidakis, N. *et al.* Temperature dependence of the electron diffusion coefficient in electrolyte-filled TiO_2 nanoparticle films: evidence against multiple trapping in exponential conduction-band tails. *Phys. Rev. B* **73,** 045326 (2006).
4. Varghese, O. K., Paulose, M. & Grimes, C. A. Long vertically aligned titania nanotubes on transparent conducting oxide for highly efficient solar cells. *Nature Nanotech.* **4,** 592–597 (2009).
5. Kuang, D. *et al.* Application of highly ordered TiO_2 nanotube arrays in flexible dye-sensitized solar cells. *ACS Nano* **2,** 1113–1116 (2008).
6. Shankar, K. *et al.* Highly efficient solar cells using TiO_2 nanotube arrays sensitized with a donor-antenna dye. *Nano Lett.* **8,** 1654–1659 (2008).
7. Kim, D., Ghicov, A., Albu, S. P. & Schmuki, P. Bamboo-type TiO_2 nanotubes: improved conversion efficiency in dye-sensitized solar cells. *J. Am. Chem. Soc.* **130,** 16454–16455 (2008).
8. Zhu, K., Neale, N. R., Miedaner, A. & Frank, A. J. Enhanced charge-collection efficiencies and light scattering in dye-sensitized solar cells using oriented TiO_2 nanotubes arrays. *Nano Lett.* **7,** 69–74 (2007).
9. Jennings, J. R., Ghicov, A., Peter, L. M., Schmuki, P. & Walker, A. B. Dye-sensitized solar cells based on oriented TiO_2 nanotube arrays: transport, trapping and transfer of electrons. *J. Am. Chem. Soc.* **130,** 13364–13372 (2008).
10. Beard, M. C., Turner, G. M. & Schmuttenmaer, C. A. Transient photoconductivity in GaAs as measured by time-resolved terahertz spectroscopy. *Phys. Rev. B* **62,** 15764–15777 (2000).
11. Baxter, J. B. & Schmuttenmaer, C. A. Conductivity of ZnO nanowires, nanoparticles and thin films using time-resolved terahertz spectroscopy. *J. Phys. Chem. B* **110,** 25229–25239 (2006).
12. Turner, G. M., Beard, M. C. & Schmuttenmaer, C. A. Carrier localization and cooling in dye-sensitized nanocrystalline titanium dioxide. *J. Phys. Chem. B* **106,** 11716–11719 (2002).
13. Gong, D., Grimes, C. A. & Varghese, O. K. Titanium oxide nanotube arrays prepared by anodic oxidation. *J. Mater. Res.* **16,** 3331–3334 (2001).
14. Varghese, O. K., Paulose, M., LaTempa, T. J. & Grimes, C. A. High-rate solar photocatalytic conversion of CO_2 and water vapor to hydrocarbon fuels. *Nano Lett.* **9,** 731–737 (2009).
15. Mor, G. K., Varghese, O. K., Paulose, M., Shankar, K. & Grimes, C. A. A review on highly ordered, vertically oriented TiO_2 nanotube arrays: fabrication, material properties and solar. *Sol. Energy Mater. Sol. Cells* **90,** 2011–2075 (2006).
16. Shankar, K. *et al.* Recent advances in the use of TiO_2 nanotube and nanowire arrays for oxidative photoelectrochemistry. *J. Phys. Chem. C* **113,** 6327–6359 (2009).
17. Richter, C. *et al.* Effect of potassium adsorption on the photochemical properties of titania nanotube arrays. *J. Mater. Chem.* **19,** 2963–2967 (2009).
18. Macak, J. M. *et al.* TiO_2 nanotubes: self-organized electrochemical formation, properties and applications. *Curr. Opin. Solid State Mater. Sci.* **11,** 3–18 (2007).
19. Nemec, H., Kuzel, P. & Sundstrom, V. Far-infrared response of free charge carriers localized in semiconductor nanoparticles. *Phys. Rev. B* **79,** 115309 (2009).
20. Tiwana, P., Parkinson, P., Johnston, M. B., Snaith, H. J. & Herz, L. M. Ultrafast terahertz conductivity dynamics in mesoporous TiO_2: influence of dye sensitization and surface treatment in solid-state dye-sensitized solar cells. *J. Phys. Chem. C* **114,** 1365–1371 (2010).
21. Smith, N. V. Drude theory and optical properties of liquid mercury. *Phys. Lett. A* **26,** 126–127 (1968).
22. Smith, N. V. Classical generalization of the Drude formula for the optical conductivity. *Phys. Rev. B* **64,** 155106 (2001).
23. Kaindl, R. A., Carnahan, M. A., Hagele, D., Lovenich, R. & Chemla, D. S. Ultrafast terahertz probes of transient conducting and insulating phases in an electron–hole gas. *Nature* **423,** 734–738 (2003).
24. Helgren, E., Armitage, N. P. & Grüner, G. Frequency-dependent conductivity of electron glasses. *Phys. Rev. B* **69,** 014201 (2004).
25. Vishwakarma, P. N. A.C. conductivity in boron doped amorphous carbon films. *Solid State Commun.* **149,** 115–120 (2009).
26. Sekiya, T. *et al.* Defects in anatase TiO_2 single crystal controlled by heat treatments. *J. Phys. Soc. Jpn* **73,** 703–710 (2004).
27. Schwanitz, K., Weiler, U., Hunger, R., Mayer, T. & Jaegermann, W. Synchrotron-induced photoelectron spectroscopy of the dye-sensitized nanocrystalline TiO_2/electrolyte interface: band gap states and their interaction with dye and solvent molecules. *J. Phys. Chem. C* **111,** 849–854 (2007).
28. Westermark, K. *et al.* Determination of the electronic density of states at a nanostructured TiO_2/Ru-dye/electrolyte interface by means of photoelectron spectroscopy. *Chem. Phys.* **285,** 157–165 (2002).
29. Minato, T. *et al.* The electronic structure of oxygen atom vacancy and hydroxyl impurity defects on titanium dioxide (110) surface. *J. Chem. Phys.* **130,** 124502 (2009).
30. Jeong, B. S., Norton, D. P. & Budai, J. D. Conductivity in transparent anatase TiO_2 films epitaxially grown by reactive sputtering deposition. *Solid State Electron.* **47,** 2275–2278 (2003).
31. Forro, L. *et al.* High-mobility N-type charge-carriers in large single-crystals of anatase (TiO_2). *J. Appl. Phys.* **75,** 633–635 (1994).
32. Tang, H., Prasad, K., Sanjines, R., Schmid, P. E. & Levy, F. Electrical and optical properties of TiO_2 anatase thin films. *J. Appl. Phys.* **75,** 2042–2047 (1994).
33. Enright, B. & Fitzmaurice, D. Spectroscopic determination of electron and mole effective masses in a nanocrystalline semiconductor film. *J. Phys. Chem.* **100,** 1027–1035 (1996).
34. Diebold, U. The surface science of titanium dioxide. *Surf. Sci. Rep.* **48,** 53–229 (2003).
35. Mahajan, V. K., Misra, M., Raja, K. S. & Mohapatra, S. K. Self-organized TiO_2 nanotubular arrays for photoelectrochemical hydrogen generation: effect of crystallization and defect structures. *J. Phys. D* **41,** 125307 (2008).

Acknowledgements

The authors acknowledge support from the Chemical Sciences, Geosciences and Biosciences Division, Office of Basic Energy Sciences, Office of Science, US Department of Energy (DE-FG02-07ER15909) for partial support of this work.

Author contributions

C.R. and C.A.S. conceived and designed the experiments, analysed the data and co-wrote the paper. C.R. performed the experiments.

Additional information

The authors declare no competing financial interests. Supplementary information accompanies this paper at www.nature.com/naturenanotechnology. Reprints and permission information is available online at http://npg.nature.com/reprintsandpermissions/. Correspondence and requests for materials should be addressed to C.A.S.

nature nanotechnology

SUPPLEMENTARY INFORMATION

DOI: 10.1038/NNANO.2010.196

Exciton-like trap states limit electron mobility in TiO_2 nanotubes

Christiaan Richter and Charles A. Schmuttenmaer*

*Electronic mail: charles.schmuttenmaer@yale.edu

July 28, 2010

Contents

DOI: 10.1038/NNANO.2010.196

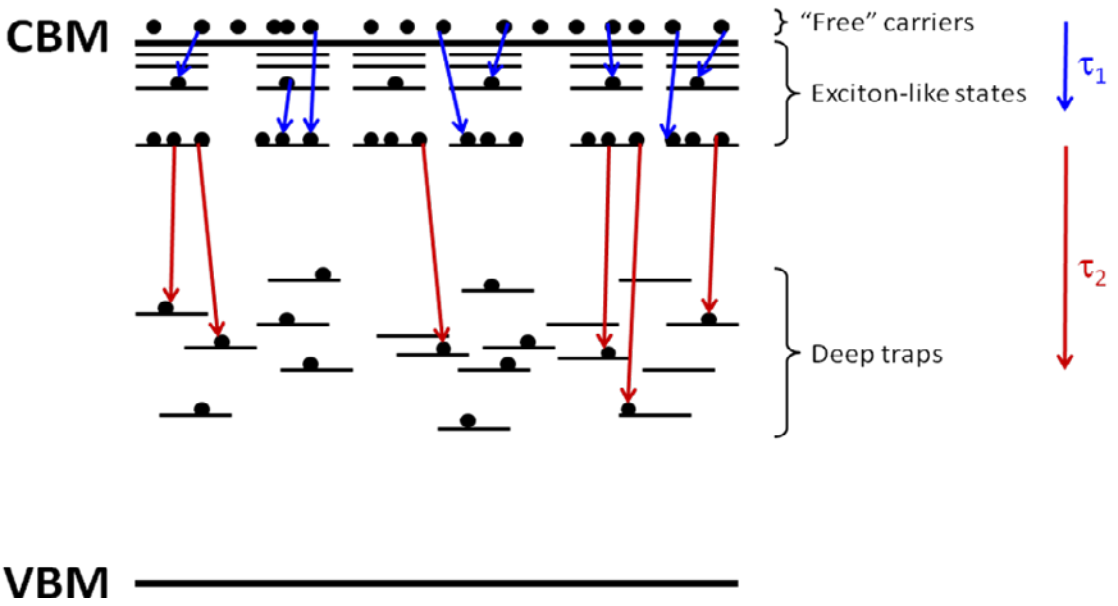

Figure S1. Schematic representation of measurement. Photoexcitation of dye sensitized TiO_2 nanotubes produces "free" carriers which then populate exciton-like states on a time scale of τ_1. This is followed by relaxation to deep traps on time scale τ_2, where $\tau_1 < \tau_2$. The time scales are 5 to 20 ps for τ_1, and 10 to 40 ps for τ_2, and they depend on the conditions under which the samples were fabricated and photoexcited.

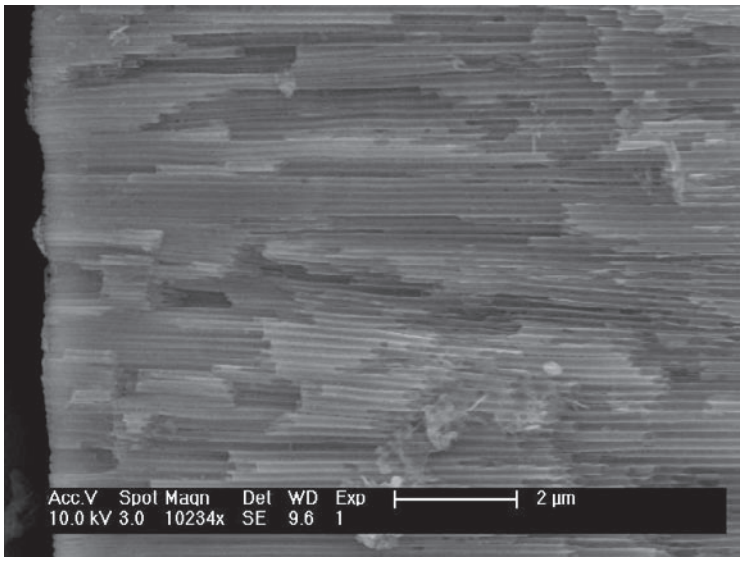

Figure S2. A side-view SEM image of a NT sample. The open 'top-side' of the nanotube array is on the left of the image.

Fitting equations and parameters

The equations used to model the data are given here. The parameter values obtained for samples prepared and/or probed under different conditions are given in Tables S1 – S3.

Drude conductivity[1,2]

$$\sigma_{Drude}(\omega) = \frac{\sigma_0}{1 - i\omega\tau} \quad \text{where} \quad \sigma_0 = \frac{N_e e^2 \tau}{m_e^*} \tag{S1}$$

Where ω is frequency (rad/s), τ is scattering time, i is unit imaginary, N_e is electron density, e is the charge of an electron, and m_e* is the carrier's effective mass. The Drude model is the simplest model of conductivity. It assumes complete momentum randomization after each scattering event.

Drude-Smith conductivity[3]

$$\sigma_{DS}(\omega) = \frac{\sigma_0}{1 - i\omega\tau}\left(1 + \frac{c}{1 - i\omega\tau}\right) \quad c \in [-1,1] \tag{S2}$$

There is a single parameter, c, beyond the standard Drude model, which is referred to as the persistence of velocity parameter. When $c = 0$, the Drude model is recovered. When c approaches –1, the low frequency and DC conductivity is suppressed, and the imaginary conductivity becomes negative at intermediate frequencies.

Power law conductivity[4]

$$\sigma_{PL}(\omega) = A\left(i\frac{\omega}{\omega_s}\right)^{\alpha} \tag{S3}$$

This is a Kramers-Kroning consistent implementation of power law behavior where ω_s is an arbitrary frequency scale. Here we choose $\omega_s = 2\pi \cdot 1$ THz.

Lorentz oscillator[2]

$$\varepsilon_{LO}(\omega) = \varepsilon_R + \Delta\varepsilon \frac{\omega_0^2}{\left(\omega_0^2 - \omega^2\right) - i\gamma\omega} \tag{S4}$$

with $\Delta\varepsilon = (\varepsilon_L - \varepsilon_R)$. Where ε_L is the relative dielectric constant for $\omega << \omega_0$ and ε_R is the relative dielectric constant for $\omega >> \omega_0$. If there are no additional resonant features between the resonant frequency and DC then $\varepsilon_L = \varepsilon_{DC}$. In the hypothetical situation where there are no additional resonant features for $\omega > \omega_0$ then ε_R would be ε_∞ ($\varepsilon \to \varepsilon_\infty$ as $\omega \to \infty$). For a classical Coloumbic Lorentz oscillator between two charges e, the oscillator strength $\Delta\varepsilon$ is given by:[2]

$$\Delta\varepsilon = \frac{N_{os} e^2}{\varepsilon_0 m_e \omega_0^2} \tag{S5}$$

where N_{os} is the number density of oscillators, and m_e in general is the reduced mass of the oscillator. In our case, assuming a stationary Ti^{4+}* entity, m_e is the electron effective mass in anatase. In the limit of ω_0 much greater than γ, the full width at half maximum (FWHM) of the peak is given by[2] FWHM = $\gamma / 2\pi$. ε_0 is the permittivity of free space.

Note that the Lorentz oscillator is not a conductivity model, but will manifest itself in the photoconductivity spectrum through the relation[5]

DOI: 10.1038/NNANO.2010.196

$$\eta(\omega) = \varepsilon(\omega) + \frac{i\sigma(\omega)}{\varepsilon_0 \omega}, \tag{S6}$$

where η is the generalized permittivity, ε is the permittivity due to bound charges, and σ is the conductivity. This expression follows directly Maxwell's equations and η characterizes the interaction of light with both bound and unbound charges.

In THz spectroscopy, the dark permittivity (η) is measured by probing the non-photoexcited sample. Subsequently, the change in permittivity upon photoexcitation ($\Delta\eta = \eta_{\text{light}} - \eta_{\text{dark}}$) is measured giving, in the most general case,

$$\Delta\eta(\omega) = \Delta\varepsilon(\omega) + \frac{i\Delta\sigma(\omega)}{\varepsilon_0 \omega}. \tag{S7}$$

At this point, it is typically assumed that the conductivity in the absence of photoexcitation is zero[†] (i.e., $\Delta\sigma = \sigma_{\text{light}} - \sigma_{\text{dark}} \approx \sigma_{\text{light}} \equiv \sigma$) and that the static permittivity does not change upon photoexcitation ($\Delta\varepsilon \approx 0$). With these assumptions (S7) becomes

$$\Delta\eta(\omega) = \frac{i\sigma(\omega)}{\varepsilon_0 \omega}$$

or rearranging

$$\sigma_1 = \varepsilon_0 \omega \Delta\eta_2$$
$$\sigma_2 = -\varepsilon_0 \omega \Delta\eta_1.$$

Hence in the typical case (of which the NP films in this study is an example), plotting the photoconductivity $\sigma = -i\varepsilon_0 \omega \Delta\eta$ gives directly the real and imaginary parts of the conductivity

However, if the static permittivity does change upon photoexcitation, as is the case with the NT samples, then $\Delta\varepsilon$ will appear also in the photoconductivity spectrum. That is, in the more general case plotting $-i\varepsilon_0 \omega \Delta\eta$ will give a "photoconductivity spectrum" (simply denoted by $\sigma = \sigma_1 + i\sigma_2$, as is conventional) that contains contributions both from permittivity (bound charges) and conductivity (free charges):

$$\sigma \equiv -i\varepsilon_0 \omega \Delta\eta = -i\varepsilon_0 \omega \Delta\varepsilon + \Delta\sigma \tag{S8}$$

This leads to the resonant feature in Figure 2 of the main text and Figures S3, S4, S6, and S7 of the SI.

[†] If the dark conductivity is not negligible, it can be lumped in with the static permittivity. In this case a photoexcited pump-probe experiment as used here would, strictly speaking, measure *photo*conductivity which is often denoted by $\Delta\sigma$. However in nano-TiO_2 the dark conductivity is sufficiently low so that we have $\Delta\sigma = \sigma - \sigma_{\text{dark}} \approx \sigma$, and we may simply use σ for the optically measured conductivity.

Fitting parameters (400 ºC with red dye)

Using σ_{PL} (Equation S3) and a Lorentz oscillator (Equation S4), the fitting parameters corresponding to Figure 3 of the main text (sample annealed at 400 ºC for 6 h and stained with N3 dye) are given in Table S1.

time (ps)	ω_0 (THz)	γ (THz)	$\Delta\varepsilon$	ε_R	A (S/m)	α	N_{os} 10^{14} cm^{-3}
0.2	1.851779	0.841849	0.001047	0.014	0.624373	0.638153	1.781354
0.35	1.842975	1.458294	0.00225	0.014	0.841089	0.484984	3.791307
0.5	1.794364	1.36422	0.002179	0.014	1.074229	0.407041	3.48071
0.75	1.799049	1.775081	0.003632	0.014	0.946022	0.296839	5.833004
1	1.765041	1.837472	0.005219	0.014	0.805161	0.485939	8.067931
2	1.755998	2.069118	0.006774	0.014	1.012724	0.558507	10.36405
4	1.782484	2.446978	0.006141	0.014	0.838482	0.412029	9.680538
7	1.745165	2.677314	0.005399	0.014	0.55025	0.446933	8.159263
21	1.782018	1.931302	0.003617	0.014	0.582213	0.471728	5.698698

Table S1. Parameters obtained using Equations S3 and S4. The apparent oscillator density (N_{os}) is calculated using Equation S5 and an electron effective mass of 4 m_0. The value of ε_R was held fixed during fitting procedure.

DOI: 10.1038/NNANO.2010.196

Photoconductivity and fitting parameters (475 ºC with red dye)

The photoconductivity spectra of a sample annealed at 475 ºC for 1h, stained with N3 dye (red dye) and photoexcited at 400 nm is given below.

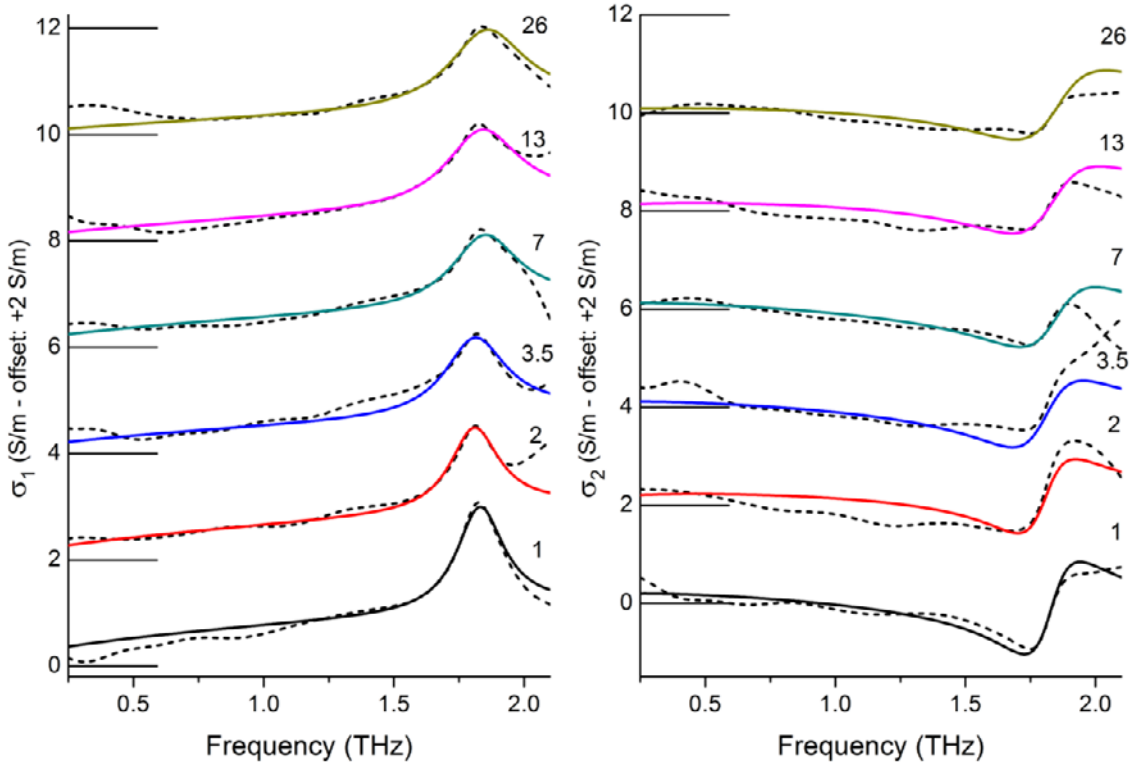

Figure S3. A sample annealed at 475 ºC for 1h & stained with N3 dye (excitation: 400 nm). The fit was done using σ_{PL} (Equation S3) and a Lorentz oscillator (Equation S4). Fitting parameters are given in Supplemental Table **S2**.

Using σ_{PL} (Equation S3) and a Lorentz oscillator (Equation S4), the fitting parameters corresponding to Figure S3 are given in Table S2.

time (ps)	ω_0 (THz)	γ (THz)	$\Delta\varepsilon$	ε_R	A (S/m)	α	N_{os} 10^{14} cm^{-3}
1	1.830775	1.395497	0.002333	0.012	1.116792	0.524963	3.879604
2	1.809464	1.434605	0.00194	0.012	1.162299	0.62213	3.151407
3.5	1.812902	1.811356	0.00228	0.012	0.900353	0.617269	3.718878
7	1.850561	1.958221	0.002145	0.012	0.93118	0.592046	3.645514
13	1.840836	2.166827	0.002568	0.012	1.041049	0.718271	4.318054
26	1.858725	2.237991	0.002657	0.012	0.936324	0.767144	4.555393

Table S2. Fitting parameters when using Equations S3 and S4. The oscillator density (N_{os}) is calculated using Equation S5 and an electron effective mass of 4 m_0. The oscillator line width or scattering rate (γ) for this sample (annealed at 475 ºC) is comparable to that for the sample annealed at 400 ºC (Table S1). In both cases γ increases over the first 10 ps to ~2.2 THz. The number of oscillators is lower and conductivity higher for the sample annealed at 475 ºC suggesting that the higher annealing temperature may have eliminated some of the defects inhibiting conductivity and/or responsible for the resonant THz absorption. The value of ε_R was held fixed during fitting procedure.

Photoconductivity and fitting parameters (475 ºC with black dye)

The photoconductivity spectra of a sample annealed at 475 ºC for 1h, stained with N749 dye (black dye) and photoexcited at 800 nm is given below.

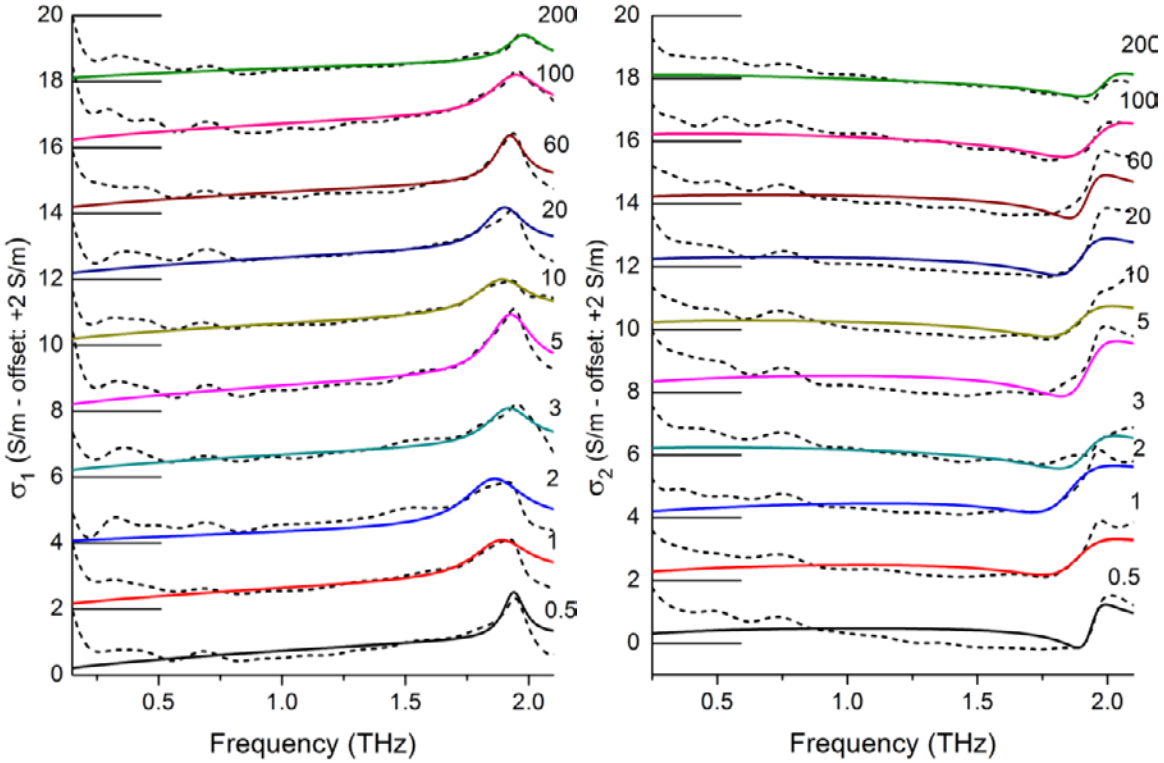

Figure S4. Photoconductivity of sample annealed at 475 ºC for 1h & stained with N749 dye (excitation: 800 nm). The solid lines are fits using σ_{PL} (Equation S3) and a Lorentz oscillator (Equation S4).

Using σ_{PL} (Equation S3) and a Lorentz oscillator (Equation S4), the fitting parameters corresponding to Figure S4 are given in Table S3.

time (ps)	ω_0 (THz)	γ (THz)	$\Delta\varepsilon$	ε_R	A (S/m)	α	N_{os} 10^{14} cm^{-3}
0.5	1.94	0.676	0.0007	0.012	1.405	0.651	1.33
1	1.89	1.753	0.0016	0.012	1.427	0.711	2.75
2	1.86	1.853	0.0021	0.012	1.325	0.838	3.67
3	1.92	1.421	0.0012	0.012	1.149	0.599	2.21
5	1.92	1.340	0.0018	0.012	1.529	0.664	3.31
10	1.89	1.628	0.0013	0.012	1.205	0.637	2.36
20	1.90	1.255	0.0012	0.012	1.238	0.645	2.13
60	1.92	0.899	0.0010	0.012	1.193	0.636	1.78
100	1.95	1.610	0.0014	0.012	1.161	0.577	2.62
0.5	1.94	0.676	0.0007	0.012	1.405	0.651	1.33

Table S3. Fitting parameters of the photoconductivity of a sample annealed at 475 ºC and stained with N749 using 800 nm photoexcitation. The value of ε_R was held fixed during fitting procedure. The oscillator density (N_{os}) is calculated using Equation S5 and an electron effective mass of 4 m_0.

DOI: 10.1038/NNANO.2010.196

Anatase energy level diagram

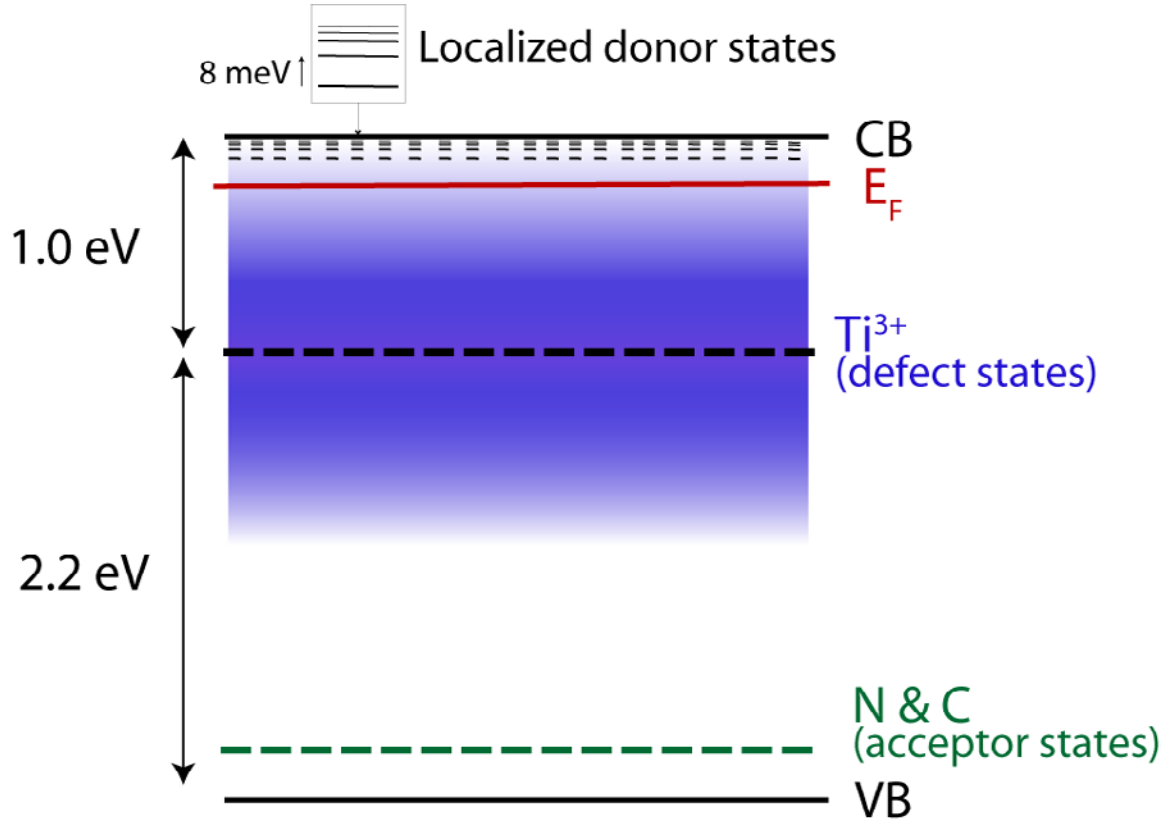

Figure S5. Energy level diagram for anatase TiO_2 nanotubes. There are Ti^{3+} defect states with an isolated ground state energy ~1 eV below the conduction band edge (CBE). The impurity band that results from the mixing of these states is shown in blue. In anatase NPs this mixing typically lifts the Fermi energy up to the CBE[6,7]. In addition to the oxygen vacancies, interstitial Ti, and F^- ions responsible for Ti^{3+} sites, the anodic NTs studied here also contain p-type dopants in the form N and C atoms. Theoretical and experimental evidence suggest that the energy of these acceptor sites will be very close to (or mixed with) the VBE. The presence of these acceptor states will result in a Fermi level that is lower in compensated NTs than it is in uncompensated NP samples. In NTs the Fermi level (E_F) may even be below the ground state energy of shallow donor states, as indicated in this diagram. Finally, localized shallow donor states are indicated. The fact that a single strong sharp resonance with an energy of ~8 meV is seen in NT samples after photoexcitation suggests that there is a large number of electrons trapped/bound in these states after electron injection/photoexcitation.

Temporal evolution of the resonant peak at ~1.8 THz

The resonance in the photoconductivity spectra of all N3 dye stained samples show relaxation dynamics illustrated in Figures S6 and S7. As seen in Figure S6, the resonance in the real conductivity at around 1.8 THz rapidly reaches a maximum within less than 2 ps after photoexcitation, and then subsequently relaxes to a plateau value just under two thirds the maximum over the next 10 ps.

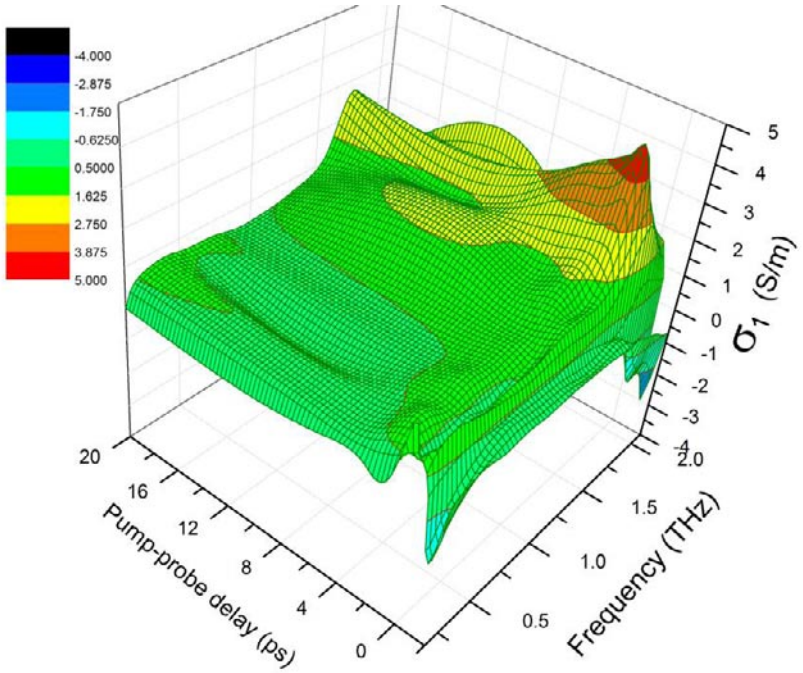

Figure S6. A 3D plot of the real part of photoconductivity of the NT sample annealed at 400 °C, stained with red dye, and photoexcited with 400 nm pump pulse at pump-probe delay time = 0 ps. Note that the resonance at 1.8 THz rapidly reaches a peak value within 1 to 2 ps.

Figure S7 shows a cut through this surface at ~1.8 THz for the samples annealed at 400 °C and 475 °C. The exact frequency chosen for each sample is that which corresponds to the peak value of the real conductivity. They have been normalized for easier comparison, but the inset shows the non-normalized spectra where it is seen that the sample annealed at 400 °C has a slightly larger peak value. Also, this figure differs from Figure 4 in the main text in that Figure S7 is simply a cut through the time-dependent real conductivity at ~1.8 THz, while Figure 4 is the value of γ, the scattering rate parameter for the Lorentzian oscillator (as given in Equation S4), found in Tables S1 and S2.

Difference in resonant peak intensity as a function of annealing temperature

As seen in the inset in Figure S7, the resonant feature in the photoconductivity spectrum of NT samples annealed at 400 ºC is more intense ($\sigma_{1,max}(\omega)$ = 4.4 S/m) than that of samples annealed at 475 ºC ($\sigma_{1,max}(\omega)$ = 3.0 S/m).

DOI: 10.1038/NNANO.2010.196

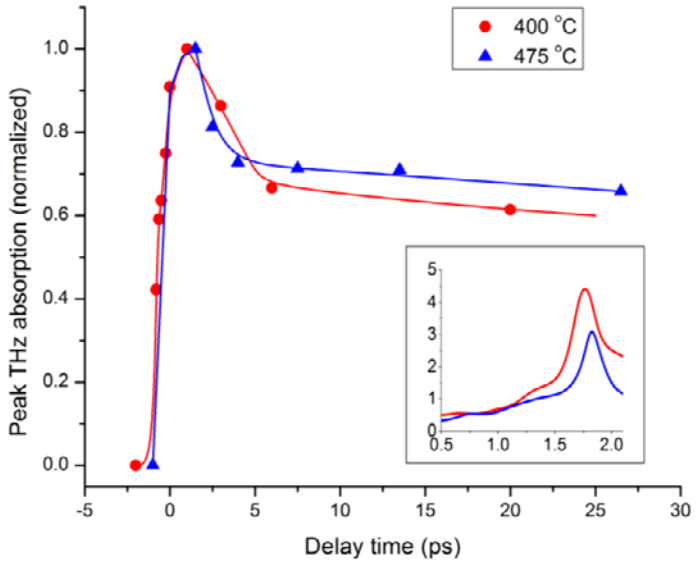

Figure S7. The normalized peak intensity of $\sigma_1(\omega)$ (at $\omega_0 \approx 1.8$ THz) as a function of time after photoexcitation. The samples are NT films stained with N3 dye after annealing at 400 ºC (red circles) or 475 ºC (blue triangles). The inset shows $\sigma_1(\omega)$ for each sample at the delay time when the resonant peak is at its maximum (~2 ps for both samples). The vertical axis of the inset is $\sigma_1(\omega)$ in S/m and the horizontal axis is frequency in THz.

By combining Equations S4 and S8, and separating real and imaginary parts we see that:

$$\sigma_1(\omega) = \varepsilon_0 \omega \Delta\varepsilon_2 + \Delta\sigma_1$$

$$= \varepsilon_0 \omega \varepsilon_{LO,2} + \sigma_{PL,1} \qquad \text{(using the LO and PL models described above)}$$

$$\approx \varepsilon_0 \omega \varepsilon_{LO,2} \qquad \text{for } \omega \to \omega_0 \qquad \text{(neglecting the contribution from } \sigma_{PL}\text{)}$$

$$= \varepsilon_0 \gamma \omega^2 \Delta\varepsilon \frac{\omega_0^2}{\left(\omega_0^2 - \omega^2\right) + \left(\gamma\omega\right)^2} .$$

The resonant peak occurs when $\omega = \omega_0$, and its height will be given by:

$$\sigma_1(\omega_0) = \frac{\varepsilon_0 \Delta\varepsilon \omega_0^2}{\gamma} .$$

Upon substitution of Equation S5, one obtains

$$\sigma_1(\omega_0) = \frac{N_{os}}{\gamma} \frac{e^2}{m_e} . \qquad \text{(S9)}$$

It can be seen in Figure 4 (or tables S1 and S2) that γ is larger for samples annealed at 400 °C than for samples annealed at 475 °C. Therefore, the average lifetime of oscillators within the first 20 ps after carrier injection is shorter in the less crystalline/ordered material (400 °C) than in the material annealed at 475 °C. However, through Equation S9, this also suggests that the resonant peak height for the 400 °C annealed samples should be lower than the peak for the 475 °C annealed samples. This however is not the case (as can be seen in the inset of Figure S7). The decrease in peak intensity due to broadening is more than offset by the 400 °C samples also having a higher defect density, and hence oscillator density: $N_{os,400\,°C} \approx 10 \times 10^{14}$ cm^{-3} compared to $N_{os,475\,°C} \approx 3 \times 10^{14}$ cm^{-3} (see Tables S1 and S2).

Thus, samples annealed at lower temperature have 1) a higher defect density that results in a higher a density of oscillator states, with 2) shorter lifetimes/higher scattering rates, and 3) faster equilibration between the lattice, defect states and injected hot carriers (see Figure 4).

DOI: 10.1038/NNANO.2010.196

Differences between NTs and NPs

The differences in their spectra are real

As can be seen in the spectra given in Figure 2 of the main text, we are able to reliably measure the nanoparticle (NP) spectra up to 1.6 THz and the nanotube (NT) spectra up to 2.1 THz. The reason for this difference in spectral coverage is that we are able to fabricate free standing NT films. In contrast, the NP films are supported on 150 μm thick microscope slide cover-slips made of borosilicate glass. The associated reflection and absorption, which increases rapidly with increasing frequency, limits the bandwidth with which we can probe the NP films.

It may be tempting to assert that there could be a peak in the NP spectrum, and we simply do not have enough bandwidth to observe it. However, this is not the case. As can be seen in the NT spectrum in Figure 2 of the main text, a sharp resonance centered at 1.8 THz requires that the imaginary conductivity, $\sigma_{2,NP}(\omega)$, be negative and have negative slope over all frequencies up to 1.6 THz. This is simply not observed in the spectrum of the NP sample.

All NP films probed to date by us and others[8-15] do not show this behavior that would be consistent with the presence of a resonance but instead have characteristic Drude-Smith behavior; that is $\sigma_{2,NP}(\omega)$ has a minimum at the same frequency that $\sigma_{1,NP}(\omega)$ has its inflection point. These qualitative observations are confirmed by the excellent match of the very different conductivity models and the measured spectra (between Drude-Smith and the NP data and Lorentz oscillator and the NT data) as presented in the manuscript. Attempts to model the NP spectra with a Lorentz oscillator model fail miserably.

When performing TRTS, one is seldom fortunate enough to have the central frequency of a resonant feature fall within the accessible spectroscopic window as it does for the NT samples (notable exceptions are excitons in GaAs quantum wells[16,17] and in Cu_2O[18]). In fact, it is relatively common to infer the existence of resonances with a central frequency at significantly higher frequencies than the spectroscopically accessible spectral region. An example is the detection of excitons in ZnO that has a FIR resonance centered at ~8 THz, the presence of which is clearly seen in spectra taken only over the region 0.35 – 1.45 THz[19]. In the light of these considerations, it is clear that the photoconductivity spectra of the NT samples have a significant resonance centered at 1.8 THz and the NP samples do not (or if such resonance exists, it is a factor of 30 or more smaller than in the NTs).

Lastly, and perhaps most importantly, the absence of a peak in the conductivity spectrum of NP films is confirmed by a recently published study[15]. Tiwana et al. probed anatase NP films with TRTS on a Z-cut quartz substrate, which absorbs far less strongly than glass, and obtained spectra up to 2 THz. Their published spectrum indeed conforms to Drude-Smith behavior in perfect agreement with our spectra, and has no resonance either at 1.8 THz or anywhere else within the 0.2 – 2 THz spectral range probed.

The Fermi level and 'dark' resonant population

To first order, the intensity of a resonant feature in the photoconductivity spectrum depends on the population of resonant species. However, more precisely, the intensity in the photoconductivity spectrum ($\hat{\sigma} = \sigma_{light} - \sigma_{dark}$) of an exciton-like species such as Ti^{4+*}/e^- scales with the *increase* of the Ti^{4+*}/e^- population upon photoexcitation. Hence the equilibrium populations of

this species in the dark will also impact the intensity of an observed resonance. If the dark Fermi level is much higher than the Ti^{4+*}/e^- binding energy (E_F > CBE), then most Ti^{4+*} states will already be reduced in the dark, resulting in very little further enhancement of any of their resonances upon electron injection/photoexcitation since $[Ti^{4+*}/e^-]_{dark} \approx [Ti^{4+*}/e^-]_{photo\text{-}excited}$. Therefore, in the case of E_F > CBE there will be no resonance in the photoconductivity spectrum, even if the Ti^{3+} density is substantial.

Presence of p-type dopants in NTs

The ~1.8 THz resonance observed in all TiO_2 NT samples has not been observed in any TiO_2 NP films. This suggests that NPs have a lower Ti^{3+} state density compared to NTs. As discussed in the main text, the most likely reasons that the NTs have higher Ti^{3+} state concentrations lie in their unique fabrication conditions. However, as described in the previous paragraph, the intensity of a resonance in the photoconductivity spectrum also depends on the dark equilibrium population of the resonant state, which in turn depends on the dark Fermi level.

In addition to the n-type donor defects discussed in the main text, the NTs also contain small amounts of the p-type dopants nitrogen and carbon. Elemental analysis (see SI in McNamara et al.[20] for experimental procedures) of the annealed NT samples prior to sensitization revealed roughly 0.12 wt% C and ~0.03 wt% N (consistent with the findings of Varghese et al.[21]). Some of these atoms may be present in the form of substitutional nitrogen and/or carbon.[21-23] Therefore, anodic titania NTs fabricated in organic electrolytes may have a Fermi level somewhat lower than that of a typical NP film. NP films, which are generally pure n-type, have an experimentally observed dark Fermi level that usually resides slightly above the CBE[6,7]. Thus one would expect a relatively high fraction of any Ti^{4+*} states present in NPs to be reduced, even in the dark. If the NTs on the other hand are a compensated n-type semiconductor, this could lead to the NTs having a lower dark Fermi level compared to NPs, and therefore a more strongly enhanced resonance in their photoconductivity spectrum.

DOI: 10.1038/NNANO.2010.196

Relevance to DSSCs

In contrast to dry films probed in this study, photoanodes in functioning DSSCs are immersed in a redox electrolyte, and the dark Fermi level in functioning DSSCs is determined by the iodide/triiodide couple[24]. How relevant are the insights obtained by probing dry films using TRTS to actual DSSCs? Furthermore, how important are the shallow traps in the NTs that are not present in the NPs?

The injected electron density immediately after photo-excitation in our experiments (~1×10^{17} – 5×10^{17} cm^{-3}) compare well with the extracted electron density in NP films in working DSSCs (~3×10^{17} cm^{-3} at short circuit and ~3×10^{18} cm^{-3} at open circuit)[25]. This suggests that the occupancy level of these shallow donor sites in our experiments most likely is comparable to those in actual cells. In fact, we recently showed that the injection efficiency measured by TRTS and DSSC efficiency were proportional to each other for films made with varying amounts of anatase and rutile[26]. When comparing NP films stained with different dyes, we typically find that the injection efficiency measured by TRTS correlates very strongly with DSSC efficiency.

Although macroscopic experiments reveal similar electron extraction times for NTs and NPs[27,28] the measured electron lifetimes are considerably longer in NTs compared to NPs[28-30]. It is conceivable that the same interaction with shallow donor sites that suppresses electron mobility also may play a role in reducing the rate of electron scavenging by species in the electrolyte by in effect increasing the NTs own "affinity" for electrons.

Working DSSCs employing either one of these nanomaterials have remarkably high carrier collection efficiencies (90-99%)[31]. The reason for this is that the recombination processes in DSSCs are even slower than the slow electron transfer (e.g. at ~1 sun typical measured values for the electron extraction time, τ_c, are about 1 ms, and about 10 – 100 ms for the average electron lifetime, τ_r[24,27,28,31,32]. Since collection efficiencies are already very high it is therefore not a given that improving the electron transport properties of either NT or NP films would necessarily result in a marked increase in cell performance. However, the state-of-the-art DSSC (TiO_2 NP diameter of about nm, triiodide/iodide redox couple, N719 or a close variant as the dye, additives like tert-butylpyridine etc.) has been highly refined over the years, and it would not be expected that radically changing any single component while leaving the others the same would result in a better DSSC. On the other hand, should a new nanomaterial be capable of electron transport that is orders of magnitude faster than its predecessors, such as TiO_2 NTs free of these shallow traps, it could conceivably become part of a new dye, redox couple, electrolyte and photoanode system specifically designed to exploit this property.

Time-resolved terahertz spectroscopy applied to nanostructured materials

The theory of and experimental setup for ultrafast THz generation and detection, and procedures for data workup used in time resolved THz spectroscopy (TRTS) have been discussed at length elsewhere[33-36]. TRTS is an ideal tool for studying free carrier dynamics within nanomaterials on sub-picosecond to nanosecond timescales. Carrier scattering times are often on the 15 to 200 fs time scale, which leads to a peak in the imaginary conductivity in the range of 0.75 to 10 THz, thereby allowing the electrical conductivity of a sample to be quantitatively determined without making physical contact with the sample. Thus, even carriers localized within nanostructures can be studied. Upon propagation through the sample, the THz probe pulses undergo both a wavelength dependant delay and attenuation based on its optical properties. Free carrier interactions, excitons, and IR active phonons (if present) can all affect the optical properties. Since the full electric field amplitude of the THz pulses is measured and mapped out (see Figure S8), rather than the power only, *both* the refractive index (which governs the delay of pulses) and absorption coefficient is measured over the probe bandwidth. This is then attributed to a change in the permittivity and/or conductivity of the sample upon photoexcitation. In short, TRTS is a noncontact electrical probe with sub-picosecond time resolution.

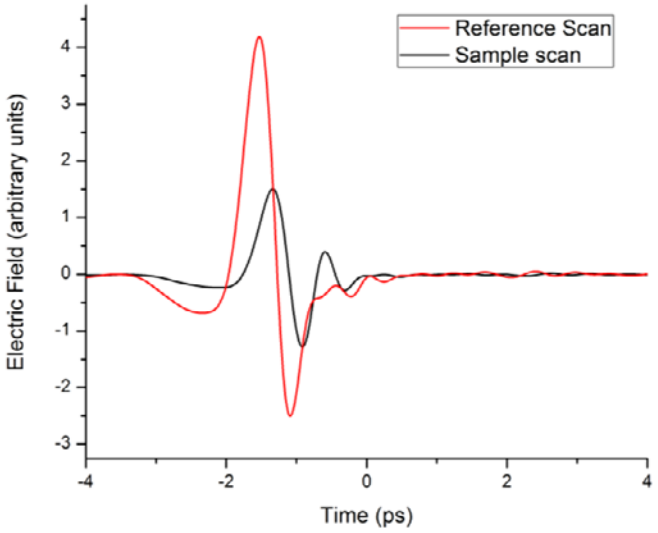

Figure S8. The electric field of a typical THz probe pulse. Shown is a reference pulse (red) propagated through free space, and a pulse that was transmitted through a non-photoexcited NT sample (black). Note that the pulse is both attenuated by absorption and delayed due to the sample's refractive index. The bandwidth of these pulses is roughly 0.2 – 2.5 THz.

We will highlight a only a few relevant points regarding the application of TRTS to nanomaterials such as TiO_2 NTs; a more comprehensive treatment can be found in Reference 37. The probe wavelength of 100 μm – 1 mm, depending on the specifics of any particular apparatus, is more than 3 orders of magnitude larger than the typical morphological dimensions of individual nanostructures such as nanotubes, nanowires, nanorods, nanoparticles, etc. Therefore, probe pulses are not scattered by individual nanostructures as occurs with visible light or even infrared. Instead, the sample behaves as if it is a single homogenous medium, i.e., an effective medium, with its associated wavelength dependant absorption and refractive index. It is this refractive index that, for instance, determines the amount of reflection from the front and back interfaces of the sample. This reflection is accounted for in the analysis of the data. The porosity, or more precisely the volume fraction of semiconductor relative to air, determines the properties of the

DOI: 10.1038/NNANO.2010.196

effective medium as a function of the properties of the two constituents[37]. The porosity of a given sample can be determined by quantifying the different regions in a scanning electron micrograph of the sample.

The sample dimensions are typically 1 cm × 1 cm × x, where 1 μm ≤ x ≤ 50 μm. The diffraction limited spot size of a probe beam focused in free space, as opposed to being confined within some sort of waveguide structure, is on the order of 1 to 2 mm for the experimental apparatus used in this study. This is due to the wavelength of the low frequency spectral components in the THz pulse: 1 mm for 0.30 THz (10 cm^{-1}), and 2 mm for 0.15 THz (5 cm^{-1}). Therefore, the lateral dimensions of the samples must be at least 5 mm × 5 mm, and similarly, the photoexcitation beam must also be on the order of 5 mm diameter such that the entire sample is uniformly illuminated.

The optimum sample thickness, which typically ranges from 1 to 50 μm, is determined solely by its optical properties. If it is highly absorbing, such as if it is a doped semiconductor, then it must be kept thin. On the other hand, it must be thick enough to show a change in transmission of 1 part in 10^4 or greater upon photoexcitation. Issues related to penetration depth and sample thickness are typically easily reconciled.

As understood from the above discussion, it is not currently possible to study individual nanostructures with TRTS. However, advances in guided waves and plasmonic enhancement are an active area in THz spectroscopy, and provide a reason to believe that this shall soon be possible.

Supplemental References

1 Ashcroft, N. W. & Mermin, D. N. *Solid State Physics*. (Saunders College, 1976).

2 Fox, M. *Optical Properties of Solids*. (Oxford University Press, 2001).

3 Smith, N. V. Classical generalization of the Drude formula for the optical conductivity. *Phys. Rev. B* **64**, (2001).

4 Helgren, E., Armitage, N. P. & Gruner, G. Frequency-dependent conductivity of electron glasses. *Phys. Rev. B* **69**, 15, (2004).

5 Greiner, W. *Classical Electrodynamics*. p. 317 (Springer, 1998).

6 Schwanitz, K., Weiler, U., Hunger, R., Mayer, T. & Jaegermann, W. Synchrotron-induced photoelectron spectroscopy of the dye-sensitized nanocrystalline TiO_2/electrolyte interface: Band gap states and their interaction with dye and solvent molecules. *J. Phys. Chem. C* **111**, 849-854, (2007).

7 Westermark, K. *et al.* Determination of the electronic density of states at a nanostructured TiO2/Ru-dye/electrolyte interface by means of photoelectron spectroscopy. *Chem. Phys.* **285**, 157-165, (2002).

8 Turner, G. M., Beard, M. C. & Schmuttenmaer, C. A. Carrier localization and cooling in dye-sensitized nanocrystalline titanium dioxide. *J. Phys. Chem. B* **106**, 11716-11719, (2002).

9 Hendry, E., Wang, F., Shan, J., Heinz, T. F. & Bonn, M. Electron transport in TiO_2 probed by THz time-domain spectroscopy. *Phys. Rev. B* **69**, (2004).

10 Hendry, E., Koeberg, M., O'Regan, B. & Bonn, M. Local field effects on electron transport in nanostructured TiO_2 revealed by terahertz spectroscopy. *Nano Lett.* **6**, 755-759, (2006).

11 Hendry, E., Koeberg, M., Pijpers, J. & Bonn, M. Reduction of carrier mobility in semiconductors caused by charge-charge interactions. *Phys. Rev. B* **75**, (2007).

12 Nemec, H., Kuzel, P. & Sundstrom, V. Far-infrared response of free charge carriers localized in semiconductor nanoparticles. *Phys. Rev. B* **79**, (2009).

13 Nemec, H. *et al.* Ultrafast terahertz photoconductivity in nanocrystalline mesoporous TiO_2 films. *Appl. Phys. Lett.* **96**, (2010).

14 Nemec, H. *et al.* Influence of the Electron-Cation Interaction on Electron Mobility in Dye-Sensitized ZnO and TiO2 Nanocrystals: A Study Using Ultrafast Terahertz Spectroscopy. *Phys. Rev. Lett.* **104**, (2010).

15 Tiwana, P., Parkinson, P., Johnston, M. B., Snaith, H. J. & Herz, L. M. Ultrafast Terahertz Conductivity Dynamics in Mesoporous TiO_2: Influence of Dye Sensitization and Surface Treatment in Solid-State Dye-Sensitized Solar Cells. *J. Phys. Chem. C* **114**, 1365-1371, (2010).

16 Lloyd-Hughes, J., Beere, H. E., Ritchie, D. A. & Johnston, M. B. Terahertz magnetoconductivity of excitons and electrons in quantum cascade structures. *Phys. Rev. B* **77**, (2008).

17 Kaindl, R. A., Carnahan, M. A., Hagele, D., Lovenich, R. & Chemla, D. S. Ultrafast terahertz probes of transient conducting and insulating phases in an electron-hole gas. *Nature* **423**, 734-738, (2003).

DOI: 10.1038/NNANO.2010.196

18 Huber, R., Schmid, B. A., Shen, Y. R., Chemla, D. S. & Kaindl, R. A. Stimulated terahertz emission from intraexcitonic transitions in Cu_2O. *Phys. Rev. Lett.* **96**, (2006).

19 Hendry, E., Koeberg, M. & Bonn, M. Exciton and electron-hole plasma formation dynamics in ZnO. *Phys. Rev. B* **76**, (2007).

20 McNamara, W. R. *et al.* Hydroxamate anchors for water-stable attachment to TiO2 nanoparticles. *Ener. Environ. Sci.* **2**, 1173-1175, (2009).

21 Varghese, O. K., Paulose, M., LaTempa, T. J. & Grimes, C. A. High-Rate Solar Photocatalytic Conversion of CO_2 and Water Vapor to Hydrocarbon Fuels. *Nano Lett.* **9**, 731-737, (2009).

22 Liu, Z. Y., Pesic, B., Raja, K. S., Rangaraju, R. R. & Misra, M. Hydrogen generation under sunlight by self ordered TiO2 nanotube arrays. *Int. J. Hydrogen Energy* **34**, 3250-3257, (2009).

23 Misra, M., Raja, K. S., Mahajan, V. K. & Mohapatra, S. K.Photo-electrochemical generation of hydrogen using hybrid titanium dioxide nanotubular arrays, in *Solar Hydrogen and Nanotechnology* Vol. 6340 *Proceedings of the Society of Photo-Optical Instrumentation Engineers (SPIE)* (ed L. Vayssieres) U128-U139 (2006).

24 Frank, A. J., Kopidakis, N. & Van de Lagemaat, J. Electrons in nanostructured TiO_2 solar cells: transport, recombination and photovoltaic properties. *Coord. Chem. Rev.* **248**, 1165-1179, (2004).

25 Koops, S. E., O'Regan, B. C., Barnes, P. R. F. & Durrant, J. R. Parameters Influencing the Efficiency of Electron Injection in Dye-Sensitized Solar Cells. *J. Am. Chem. Soc.* **131**, 4808-4818, (2009).

26 Li, G. H. *et al.* Synergistic effect between anatase and rutile TiO2 nanoparticles in dye-sensitized solar cells. *Dalton Trans.*, 10078-10085, (2009).

27 Jennings, J. R., Ghicov, A., Peter, L. M., Schmuki, P. & Walker, A. B. Dye-sensitized solar cells based on oriented TiO_2 nanotube arrays: Transport, trapping, and transfer of electrons. *J. Am. Chem. Soc.* **130**, 13364-13372, (2008).

28 Zhu, K., Neale, N. R., Miedaner, A. & Frank, A. J. Enhanced Charge-Collection Efficiencies and Light Scattering in Dye-Sensitized Solar Cells Using Oriented TiO2 Nanotubes Arrays. *Nano Lett.* **7**, 69-74, (2007).

29 Paulose, M., Shankar, K., Varghese, O. K., Mor, G. K. & Grimes, C. A. Application of highly-ordered TiO_2 nanotube-arrays in heterojunction dye-sensitized solar cells. *J. Phys. D: Appl. Phys.* **39**, 2498-2503, (2006).

30 Mor, G. K., Shankar, K., Paulose, M., Varghese, O. K. & Grimes, C. A. Use of highly-ordered TiO_2 nanotube arrays in dye-sensitized solar cells. *Nano Lett.* **6**, 215-218, (2006).

31 Ardo, S. & Meyer, G. J. Photodriven heterogeneous charge transfer with transition-metal compounds anchored to TiO2 semiconductor surfaces. *Chem. Soc. Rev.* **38**, 115-164, (2009).

32 Kopidakis, N., Benkstein, K. D., van de Lagemaat, J. & Frank, A. J. Transport-limited recombination of photocarriers in dye-sensitized nanocrystalline TiO2 solar cells. *J. Phys. Chem. B* **107**, 11307-11315, (2003).

33 Beard, M. C., Turner, G. M. & Schmuttenmaer, C. A. Transient photoconductivity in GaAs as measured by time-resolved terahertz spectroscopy. *Phys. Rev. B* **62**, 15764-15777, (2000).

34 Beard, M. C., Turner, G. M. & Schmuttenmaer, C. A. Terahertz spectroscopy. *J. Phys. Chem. B* **106**, 7146-7159, (2002).

35 Schmuttenmaer, C. A. Exploring dynamics in the far-infrared with terahertz spectroscopy. *Chem. Rev.* **104**, 1759-1779, (2004).

36 Baxter, J. & Schmuttenmaer, C. A. Time-Resolved Terahertz Spectroscopy and Terahertz Emission Spectroscopy, in *Terahertz Spectroscopy: Principles and Applications* (ed Susan L. Dexheimer) Ch. 3, 73-118 (CRC Press, 2008).

37 Baxter, J. B. & Schmuttenmaer, C. A. Conductivity of ZnO nanowires, nanoparticles, and thin films using time-resolved terahertz spectroscopy. *J. Phys. Chem. B* **110**, 25229-25239, (2006).